

# Control of Sarcoplasmic Reticulum $\text{Ca}^{2+}$ Release by Stochastic RyR Gating within a 3D Model of the Cardiac Dyad and Importance of Induction Decay for CICR Termination

M. B. Cannell,<sup>†,Δ\*</sup> C. H. T. Kong,<sup>†</sup> M. S. Imtiaz,<sup>‡</sup> and D. R. Laver<sup>†,Δ</sup>

<sup>†</sup>Department of Physiology and Pharmacology, University of Bristol, Bristol, United Kingdom; and <sup>‡</sup>School of Biomedical Sciences and Pharmacy, University of Newcastle and Hunter Medical Research Institute, Callaghan, New South Wales, Australia

**ABSTRACT** The factors responsible for the regulation of regenerative calcium-induced calcium release (CICR) during  $\text{Ca}^{2+}$  spark evolution remain unclear. Cardiac ryanodine receptor (RyR) gating in rats and sheep was recorded at physiological  $\text{Ca}^{2+}$ ,  $\text{Mg}^{2+}$ , and ATP levels and incorporated into a 3D model of the cardiac dyad, which reproduced the time course of  $\text{Ca}^{2+}$  sparks,  $\text{Ca}^{2+}$  blinks, and  $\text{Ca}^{2+}$  spark restitution. The termination of CICR by induction decay in the model principally arose from the steep  $\text{Ca}^{2+}$  dependence of RyR closed time, with the measured sarcoplasmic reticulum (SR) lumen  $\text{Ca}^{2+}$  dependence of RyR gating making almost no contribution. The start of CICR termination was strongly dependent on the extent of local depletion of junctional SR  $\text{Ca}^{2+}$ , as well as the time course of local  $\text{Ca}^{2+}$  gradients within the junctional space. Reducing the dimensions of the dyad junction reduced  $\text{Ca}^{2+}$  spark amplitude by reducing the strength of regenerative feedback within CICR. A refractory period for  $\text{Ca}^{2+}$  spark initiation and subsequent  $\text{Ca}^{2+}$  spark amplitude restitution arose from 1), the extent to which the regenerative phase of CICR can be supported by the partially depleted junctional SR, and 2), the availability of releasable  $\text{Ca}^{2+}$  in the junctional SR. The physical organization of RyRs within the junctional space had minimal effects on  $\text{Ca}^{2+}$  spark amplitude when more than nine RyRs were present. Spark amplitude had a nonlinear dependence on RyR single-channel  $\text{Ca}^{2+}$  flux, and was approximately halved by reducing the flux from 0.6 to 0.2 pA. Although rat and sheep RyRs had quite different  $\text{Ca}^{2+}$  sensitivities,  $\text{Ca}^{2+}$  spark amplitude was hardly affected. This suggests that moderate changes in RyR gating by second-messenger systems will principally alter the spatiotemporal properties of SR release, with smaller effects on the amount released.

## INTRODUCTION

In cardiac muscle, depolarization of the sarcolemma initiates  $\text{Ca}^{2+}$  release by activating sarcolemmal L-type  $\text{Ca}^{2+}$  channels, providing a local increase in cytoplasmic calcium concentration in the junctional space of the dyad (for review, see Bers (1)). This initiates  $[\text{Ca}^{2+}]$ -dependent activation of the sarcoplasmic reticulum (SR)  $\text{Ca}^{2+}$  release channels, which are ryanodine receptors (RyRs) (2,3). The subsequent release of  $\text{Ca}^{2+}$  from the SR further increases the  $[\text{Ca}^{2+}]$  in the junctional space and leads to regenerative RyR activation in a process known as calcium-induced calcium release (CICR) (4). In such a regenerative process, the larger SR  $\text{Ca}^{2+}$  flux should prevent subsequent control by the surface membrane (5) and deep-SR  $\text{Ca}^{2+}$ -store depletion. However, the quantity of  $\text{Ca}^{2+}$  released from the SR has a graded dependence on the magnitude of the  $\text{Ca}^{2+}$  influx across the sarcolemma (5,6), and the SR releases only ~50% of its content (see, e.g., Picht et al. (7)). The discovery of  $\text{Ca}^{2+}$  sparks (1,8) and local control theories (9) provided a solution to this problem by showing that graded responses can result from the spatiotemporal summation of individual  $\text{Ca}^{2+}$  release sites that are spatially uncoupled to limit regenerative behavior (10,11). However, local regeneration

in CICR during  $\text{Ca}^{2+}$  sparks might still oppose reliable  $\text{Ca}^{2+}$  spark termination (12,13).

The termination problem in the local control mechanism has been reviewed elsewhere (12,13), and several mechanisms have been proposed to limit local regeneration. For example, it has been suggested that time-, SR- $\text{Ca}^{2+}$ -, and cytosolic- $\text{Ca}^{2+}$ -dependent RyR inactivation (4–6,14–16) would dampen regenerative behavior. However, the reported rates of inactivation are much slower than the time to peak of the  $\text{Ca}^{2+}$  spark (14,16,17). Stochastic RyR gating and the rapid response of local  $[\text{Ca}^{2+}]$  to changing RyR flux may also contribute to spontaneous closure via stochastic attrition (9), although stochastic attrition on the timescale of a  $\text{Ca}^{2+}$  spark seems unlikely for more than ~5–10 RyRs in a junctional cluster. The addition of inter-RyR allosteric interactions, which effectively reduces the number of RyRs in the cluster (e.g., very strong coupling will make the cluster gate as a single channel), can allow reliable termination for larger numbers of RyRs (12,18). However, direct observations of such allosteric interactions are few, and to our knowledge, such behavior has only been seen under quite nonphysiological conditions with detergent-solubilized RyRs (19).

Depletion of the SR lumen  $[\text{Ca}^{2+}]$  may reduce the RyR release flux to the point where regenerative CICR is no longer supported (5,6,20–22), but measurements of SR  $[\text{Ca}^{2+}]$  with fluo-5N suggest only moderate SR depletion

Submitted January 15, 2013, and accepted for publication March 25, 2013.

<sup>Δ</sup>M.B. Cannell and D. R. Laver contributed equally to this work.

\*Correspondence: Mark.Cannell@bristol.ac.uk

Editor: James Sneyd.

© 2013 by the Biophysical Society  
0006-3495/13/05/2149/11 \$2.00



<http://dx.doi.org/10.1016/j.bpj.2013.03.058>

(e.g., Picht et al. (7) and Shannon et al. (23)). We recently reported that the complex interaction of stochastically gating RyRs within a 3D spatial model could produce reliable spontaneous closure without any form of RyR inactivation (24). This closure was due to induction decay, wherein the increasing RyR closed time associated with declining RyR flux (due to junctional SR depletion) prevented closed RyRs from responding to the nearby open RyRs. Further support for the idea of induction decay comes from recent experiments in which reduced RyR conductance resulted in reduced  $\text{Ca}^{2+}$  spark amplitude despite the fact that there was no change in RyR gating (21). However, our previous report did not explore the generality of the result for different dyad geometries and used only gating data from rat RyRs, which seemed relatively insensitive to cytosolic  $\text{Ca}^{2+}$  compared to data reported elsewhere in the literature (i.e.,  $K_d \sim 10 \mu\text{M}$ ).

Here, we expand on our previous study, examining the robustness of induction decay as a termination mechanism for both rat and sheep RyR gating in the presence of physiological levels of  $\text{Mg}^{2+}$  and ATP and with different dyad geometries and single-channel currents. It is important to note that the rat RyR model reproduces measured  $\text{Ca}^{2+}$  spark restitution (25) and that our measured RyR regulation by luminal  $\text{Ca}^{2+}$  has little effect on  $\text{Ca}^{2+}$  spark properties. The model also displays a  $\text{Ca}^{2+}$  spark amplitude dependence on single RyR channel current, which is similar to that recently explored using TRIS as a permeable blocking ion (21). In addition, we discuss the implications of the model for understanding the role(s) played by possible RyR gating changes and dyad restructuring.

## METHODS

### Isolation of hearts

Healthy male adult rats (Harlan Sprague-Dawley, Indianapolis, IN) were heparinized (2000 U heparin injection BP, Weddel Pharmaceuticals, London, United Kingdom) and 15 min later anesthetized with isoflurane (Laser Animal Health, Brisbane, Australia). The hearts were rapidly removed and immediately perfused via the Langendorff method with ice-cold Krebs-Henseleit buffer (in mM, 120 NaCl, 25  $\text{NaHCO}_3$ , 10 Glucose, 5 KCl, 2  $\text{MgCl}_2$ , 1  $\text{NaH}_2\text{PO}_4$ , and 2.5  $\text{CaCl}_2$ ) for 2 min until the blood was washed out. Hearts were then perfused for 5 min with warmed ( $37^\circ\text{C}$ ) and oxygenated (95%  $\text{O}_2$ , 5%  $\text{CO}_2$ ) Krebs-Henseleit buffer, after which they were snap-frozen. Sheep hearts were excised from anesthetized ewes (5% pentobarbitone (IV) followed by oxygen/halothane) and rinsed in ice-cold homogenizing buffer (20 mM imidazole and 300 mM sucrose, pH 7.4 with HCl) before snap-freezing. All hearts were snap-frozen in liquid nitrogen and stored at  $-80^\circ\text{C}$  until further use.

### SR vesicle preparation

Briefly, heart tissue was homogenized in buffer containing 10 mM imidazole, 0.5 mM dithiothreitol (DTT), 3 mM sodium azide, 0.29 M sucrose, 1  $\mu\text{g}/\text{ml}$  leupeptin, 1  $\mu\text{g}/\text{ml}$  pepstatin A, 1 mM benzamidine, 0.5 mM phenylmethylsulfonyl fluoride, and 20 mM NaF, pH 6.9 (homogenization buffer). SR vesicles were separated by centrifugation as described in the

**Supporting Methods.** The NaF inhibited phosphatases during the SR vesicle preparation. The whole procedure was carried out at  $4^\circ\text{C}$ .

### Single-channel recordings

Lipid bilayers were formed as described in the **Supporting Methods**. Lipid bilayers separated *cis* (cytoplasmic) and *trans* (luminal) compartments. Both compartments contained 250 mM  $\text{Cs}^+$  (230 mM  $\text{CsCH}_3\text{O}_3\text{S}$ , 20 mM CsCl, and 10 mM TES buffer). In the *trans* bath,  $[\text{Ca}^{2+}]$  was either 0.1 or 1 mM. The *cis* bath contained 2 mM ATP and 3 mM  $\text{MgCl}_2$  (1 mM free  $\text{Mg}^{2+}$ ), and  $\text{Ca}^{2+}$  was titrated between 1 and 500  $\mu\text{M}$  (see **Supporting Methods** for details of pH and  $\text{Ca}^{2+}$  buffering). The composition of the *cis* solution was altered by local perfusion and the composition of the *trans* solutions was altered by addition of aliquots of stock solutions. All experiments were performed at room temperature ( $21\text{--}26^\circ\text{C}$ ) and membrane potential of  $-40$  mV (lumen at ground). Before analysis, the current signal was low-pass digitally filtered at 1 kHz. Channel 3 software (N. W. Laver, [nic@niclaver.com](mailto:nic@niclaver.com)) was used to detect channel events and measure open probability ( $P_o$ ), mean open time ( $\tau_o$ ), and mean closed time ( $\tau_c$ ).

### Model geometry

The geometry of the model dyad is shown in Fig. 1. Electron micrographs suggest a large variation in dyad size and t-tubule radius (see, e.g., Franzini-Armstrong (26), Fawcett and McNutt (27), Forbes and Van Neil (28), and Forssman and Girardier (29)). In the simulations shown here, the t-tubule is a cylinder 250 nm in diameter between computational boundaries. Wrapped around its circumference, at its midpoint, is the terminal or junctional SR (j-SR), which is represented as a pancake 360 nm along the axis, 26 nm radial thickness, and 450 nm tubule circumference. RyR  $\text{Ca}^{2+}$  release channels were arranged in clusters with a nearest-neighbor separation of 31 nm on the j-SR membrane facing the t-tubule. The j-SR was connected to the network SR (n-SR) at its center. The n-SR was isotropically distributed throughout the computational volume to mimic a labyrinth of tubules occupying a volume fraction of 3.5% of the cytoplasmic volume. Model parameter values for dyad structure are given in the Table S1 in the **Supporting Material**.

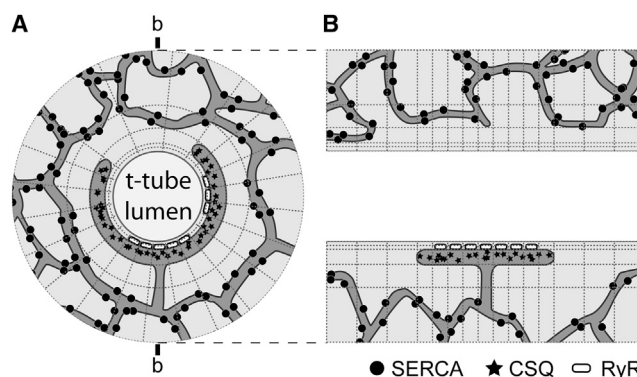


**FIGURE 1** Illustration of the model geometry. (A) Cross section of the cylindrical model with a t-tubule in the center. The j-SR wraps around the t-tubule at a 15-nm radial distance (*dyad cleft*). RyRs are located in the j-SR membrane and release  $\text{Ca}^{2+}$  into the dyad cleft. The j-SR contains calsequestrin (CSQ) and is connected to the n-SR by a tubule, which allows for  $\text{Ca}^{2+}$  diffusion between these two compartments. The SERCA  $\text{Ca}^{2+}$  uptake transporters are uniformly distributed throughout the n-SR. (B) Side view of the model in the cross section indicated by b-b in A. In this view, the t-tubule lumen runs horizontally and the j-SR can be seen on one side.

## Ion movements

Computational details are given in the [Supporting Methods](#).  $\text{Ca}^{2+}$  diffusion and binding to  $\text{Ca}^{2+}$  indicators (fluo-4 and fluo-5N) in and around the dyad were calculated using Matlab (Mathworks, Natick, MA). The ion concentrations in each volume element were calculated by solving a discretized form of the electro-diffusion/transport equation that is shown here for the case of  $\text{Ca}^{2+}$ :

$$\frac{\partial[\text{Ca}^{2+}]}{\partial t} = -D_{\text{Ca}}\nabla(\nabla[\text{Ca}^{2+}] + 2[\text{Ca}^{2+}]\nabla\Phi) + \sum_{\text{RyR}} J_{\text{RyR}} - J_{\text{SERCA}} - \sum_{\text{buffer}} J_{\text{buffer}}, \quad (1)$$

where  $D_{\text{Ca}}$  is the diffusion coefficient for  $\text{Ca}^{2+}$  and  $\Phi$  is the electrostatic potential arising from charged lipids on the t-tubule membrane. The term involving  $\nabla\Phi$  was assumed to have only radial components.  $J_{\text{RyR}}$  represents the flow of  $\text{Ca}^{2+}$  through each open RyR into the adjacent volume element in the dyad cleft (with volume  $V_{\text{cleft}}$ ), which was given by

$$J_{\text{RyR}} = \frac{i_{\text{RyR}}}{2FV_{\text{cleft}}} ([\text{Ca}^{2+}]_{j\text{-SR}} - [\text{Ca}^{2+}]_{\text{cleft}}), \quad (2)$$

where  $i_{\text{RyR}}$  is a constant to give a 0.6-pA flux (30,31) for an open RyR with a 1 mM  $[\text{Ca}^{2+}]$  gradient and  $F$  is Faraday's constant.  $\text{Ca}^{2+}$  uptake was simulated by a simplified model for sarcoendoplasmic reticulum calcium-transport ATPase (SERCA) (32) located in the n-SR, as given by

$$J_{\text{SERCA}} = \frac{K_{\text{SR,max}}}{V_{\text{cyto}}} \left( \frac{(K_{\text{SERCA}}[\text{Ca}^{2+}]_{\text{cyto}})^2}{1 + (K_{\text{SERCA}}[\text{Ca}^{2+}]_{\text{cyto}})^2} - k_{\text{leak}} \right), \quad (3)$$

where  $K_{\text{SR,max}}$  is the maximum rate of SERCA uptake,  $K_{\text{SERCA}}$  the cytoplasmic  $\text{Ca}^{2+}$  binding constant, and  $V_{\text{cyto}}$  the element volume.  $k_{\text{leak}}$  sets  $J_{\text{SERCA}}$  to zero under initial/resting conditions.  $K_{\text{SR,max}}$  was set by reproducing the rate of decline of whole-cell  $[\text{Ca}^{2+}]$  after setting cytoplasmic  $[\text{Ca}^{2+}]$  to 1  $\mu\text{M}$ , and the value is given in [Table S3](#).

$J_{\text{buffer}}$  is the contribution to  $\text{Ca}^{2+}$  fluxes from  $\text{Ca}^{2+}$  reacting with a buffer,  $B$ :

$$J_{\text{Buffer}} = k_{\text{on}}[B][\text{Ca}^{2+}] - k_{\text{off}}[CaB]. \quad (4)$$

Diffusible buffers included ATP, calmodulin, fluo-4, and fluo-5N, with diffusion coefficients described in [Table S2](#). Troponin buffering was fixed in the cytoplasmic compartment, whereas calsequestrin was fixed in the SR compartments and concentrated mainly in the j-SR. Negatively charged lipids such as phosphatidylserine (PS) and zwitterionic phosphatidylcholine (PC) give rise to a negative net charge on the lipid bilayer and provide binding sites for cations such as  $\text{Ca}^{2+}$  and  $\text{K}^{+}$ . In the model, these effects are treated using simplifying approximations, as described previously (32) (also see [Supporting Material](#)).

The equations were solved on a cylindrical coordinate system with Neumann reflective boundaries at  $\pm 2 \mu\text{m}$  along the t-tubule and at a radius of 2  $\mu\text{m}$ . Model parameters for ion diffusion and buffering are given in [Table S2](#).

## RyR gating

RyR gating was simulated using an empirical two-state (open and closed) stochastic model. The opening and closing rates were derived from two-segment linear fits to experimental transition rates (see [Fig. S1](#)), which are limited to  $\text{Ca}^{2+}$  levels during CICR and are not intended to describe RyR gating behavior at resting  $\text{Ca}^{2+}$  levels (see below). The transition rates

were calculated from the reciprocal of the empirical RyR mean closed and open times, respectively. A Monte Carlo method was used to simulate stochastic transitions of each RyR, and at the computed transition times for each RyR, the integration was restarted using the new values of  $J_{\text{RyR}}$ .

## Initiation of $\text{Ca}^{2+}$ sparks

Simulations were started either by 1- to 3-ms  $\text{Ca}^{2+}$  injection into a volume element adjacent to an RyR at a rate corresponding to 0.2 pA (to mimic an L-type  $\text{Ca}^{2+}$  channel opening) or by initializing one RyR in the open state (to mimic the initiation of a spontaneous  $\text{Ca}^{2+}$  spark). The subsequent evolution of the  $\text{Ca}^{2+}$  spark showed no difference between simulations triggered in these two ways (not shown).

## Microscope blurring

To simulate the  $\text{Ca}^{2+}$  sparks and blinks as observed by confocal microscopy, the spatial distributions of fluo-4 and fluo-5N generated by the model were convolved with 3D Gaussian point-spread function. The full width at half-maximum of the Gaussian was 0.3  $\mu\text{m}$  in the focal plane of the microscope ( $x$  and  $y$  directions) and 0.93  $\mu\text{m}$  perpendicular to the focal plane ( $z$  direction).

## RESULTS

[Fig. 2 A](#) shows the typical pattern of RyR gating observed at various cytoplasmic  $[\text{Ca}^{2+}]$  and in the presence of 2 mM ATP and 1 mM free  $\text{Mg}^{2+}$ . Under these conditions, the open probability ( $P_o$ ) of RyRs from sheep ([Fig. 2 B](#), open

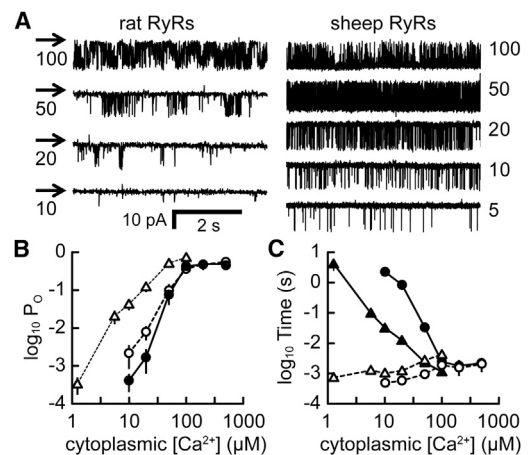


**FIGURE 2**  $[\text{Ca}^{2+}]$ -dependent RyR2 gating in lipid bilayers. Both sides of the bilayer contained (in mM) 230  $\text{CsCH}_3\text{O}_3\text{S}$  and 20  $\text{CsCl}$  (pH 7.4), with 2 ATP and 3  $\text{MgCl}_2$  on the cytoplasmic side ( $[\text{Ca}^{2+}]$  as indicated). (A) Channel openings at various  $[\text{Ca}^{2+}]$  are downward deflections from the baseline (arrows). (B) Cytoplasmic  $[\text{Ca}^{2+}]$  dependence of  $P_o$  for RyRs from rat (luminal  $[\text{Ca}^{2+}]$ , 0.1 mM (solid circles) and 1 mM (open circles)) and sheep heart (luminal  $[\text{Ca}^{2+}]$ , 0.1 mM (open triangles)). Data points show the mean  $\pm$  SE for  $n = 3$ –11 (solid circles),  $n = 4$ –8 (open circles), and  $n = 2$ –14 (open triangles). Some of the rat data values have been replotted from Laver et al. (24). (C) Cytoplasmic  $[\text{Ca}^{2+}]$  dependence of sheep RyR mean open and closed durations (0.1 mM luminal  $[\text{Ca}^{2+}]$ ). Solid symbols represent closed times and open symbols open times. Sheep RyR gating is shown by triangles and rat RyR gating, replotted from Laver et al. (24), by circles.

triangles) had a much weaker dependence on  $[Ca^{2+}]$  than that of RyRs from rat at either 0.1 mM (open circles) or 1 mM (solid circles) luminal  $[Ca^{2+}]$ . The RyR  $P_o$  for both species increased to a maximum of  $\sim 0.5$  at 0.1 mM  $[Ca^{2+}]$ . The  $P_o$  for rat RyRs showed only a modest dependence on luminal  $Ca^{2+}$  levels, consistent with studies on sheep RyRs (33,34). For  $[Ca^{2+}]$  between 1 and 100  $\mu M$ , the mean  $P_o$  varied as  $\sim [Ca^{2+}]^{2.8}$  for rat (24) and  $\sim [Ca^{2+}]^{2.1}$  for sheep, which was primarily due to changes in closed time (Figs. 2 C and S1). For simplicity, we used the closed-time data at 0.1 mM SR (trans)  $[Ca^{2+}]$ , because the model showed that j-SR levels dropped to about this level during the  $Ca^{2+}$  spark, and as shown below, allowing SR  $Ca^{2+}$  to influence closed time had only minor effects on  $Ca^{2+}$  spark properties. Any extrapolation of the empirical power function(s) describing the RyR gating seen at higher  $[Ca^{2+}]$  to lower resting  $[Ca^{2+}]$  predicts a resting  $Ca^{2+}$ -spark rate that is too low and is therefore problematic. However, if the longest-closed-time data points of Fig. 2 C for rat and sheep RyRs are extrapolated to resting conditions, these data points suggest that (shorter) closed times of  $\sim 1000$  s might pertain at 0.1  $\mu M$   $[Ca^{2+}]$ . It has been estimated that a confocal microscope samples  $\sim 1.1$  release sites per  $\mu m$  scanned (35). Therefore, a 100- $\mu m$  scan line would record from  $\sim 110$  release sites (junctions), and with  $\sim 20$  RyRs in each junction, and assuming that most spontaneous RyR openings trigger a  $Ca^{2+}$  spark, the resting  $Ca^{2+}$  spark rate would be  $\sim 2$  s $^{-1}$ , in reasonable agreement with experimental observations (8,36).

### Morphology of simulated $Ca^{2+}$ sparks and blinks

We could simulate  $Ca^{2+}$  sparks and associated SR  $Ca^{2+}$  depletion signals ( $Ca^{2+}$  blinks (8)) by incorporating fluo-4 and fluo-5N  $Ca^{2+}$  indicators into the model. Fig. 3 illustrates the time course and spatial spread of  $Ca^{2+}$  sparks (Fig. 3 A) and blinks (Fig. 3 B), derived from simulations of  $Ca^{2+}$  release by an array of 21 rat RyRs triggered by a 3 ms dihydropyridine receptor (DHPR) opening after simulated optical blurring. The simulated  $Ca^{2+}$  spark is similar to those observed experimentally (see also Laver et al. (24)), with the  $Ca^{2+}$  spark having a greater spatial width than the  $Ca^{2+}$  blink (Fig. 3 C). It is notable that no triggering sparklet (37) is seen; the trigger signal is essentially lost due to the small volume of the dyad cleft and the rapid activation of the RyR cluster. Although we do not have experimental records for  $Ca^{2+}$  blinks in rat RyRs, the simulated blinks were of comparable in amplitude, duration, and spatial extent to those reported for rabbit (minimum  $F/F_o = 60 \pm 8\%$ , full duration at half-maximum (FDHM) =  $175 \pm 7$  ms (38), and  $823 \pm 476$  nm (39)). The fluo-5N fluorescence signal significantly underestimated the extent of local depletion of the j-SR due to blurring of the j-SR, t-tubule, and n-SR structures by the microscope (40). The rate of recovery of the fluo-5N fluorescence signal (time constant = 80 ms)

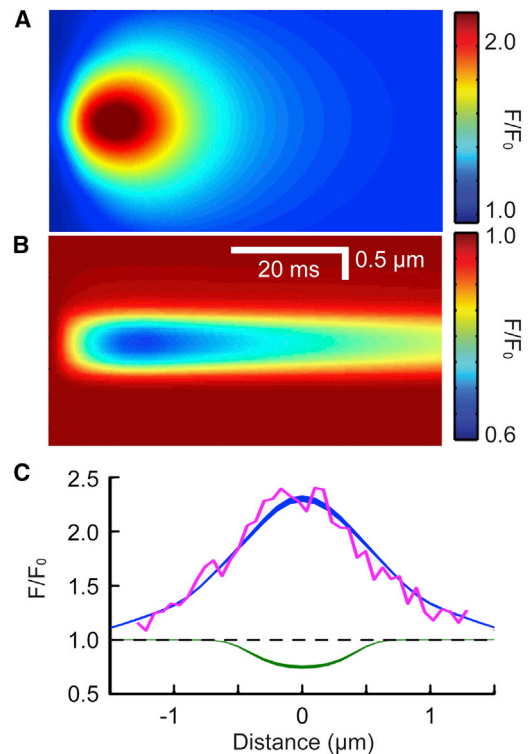


FIGURE 3 Simulation of  $Ca^{2+}$  sparks and blinks. (A) Simulated  $Ca^{2+}$  sparks. The simulated  $Ca^{2+}$  spark was generated by the array of RyRs shown in Fig. 4. (B) The corresponding simulated  $Ca^{2+}$  blink. Scale bars apply to both A and B. (C) Corresponding spatial profiles of spark and blink fluorescence at the times of their peak and minimum intensities, respectively. The noisy line shows the profile of an experimentally recorded  $Ca^{2+}$  spark (see also (23, 24) for additional comparison of model behavior to experimental data).

was substantially faster than the rate of j-SR replenishment (time constant = 180 ms), which was largely due to the saturation effects in the fluo-5N signal.

### $Ca^{2+}$ dynamics and RyR regulation during $Ca^{2+}$ sparks

Fig. 4 shows an exemplar response of the model, with 21 irregularly arranged RyRs stimulated by the DHPR-trigger opening. The time courses ( $n = 7$ ) of the computed average  $Ca^{2+}$  spark and blink signals are shown in Fig. 4 A. Mean  $[Ca^{2+}]$  in the dyad cleft and j-SR elements is shown in Fig. 4 B. The initial rise in dyad  $[Ca^{2+}]$  is due to the  $Ca^{2+}$  influx from DHPR triggering (which has no variance). Subsequent changes in  $[Ca^{2+}]$  due to stochastic RyR gating then lead to variance in both signals. Fig. 4 C shows that shortly after initiation, the number of open RyRs increased to  $\sim 10$ , which corresponds to  $P_o \sim 0.5$ , and remained at this level for  $\sim 132$  ms before the RyRs started to close; closure was complete at 22 ms. This RyR response can be understood in terms of the dyadic and j-SR  $[Ca^{2+}]$  (Fig. 4 B). Initially, dyad  $[Ca^{2+}]$  rose to high levels resulting from a regenerative



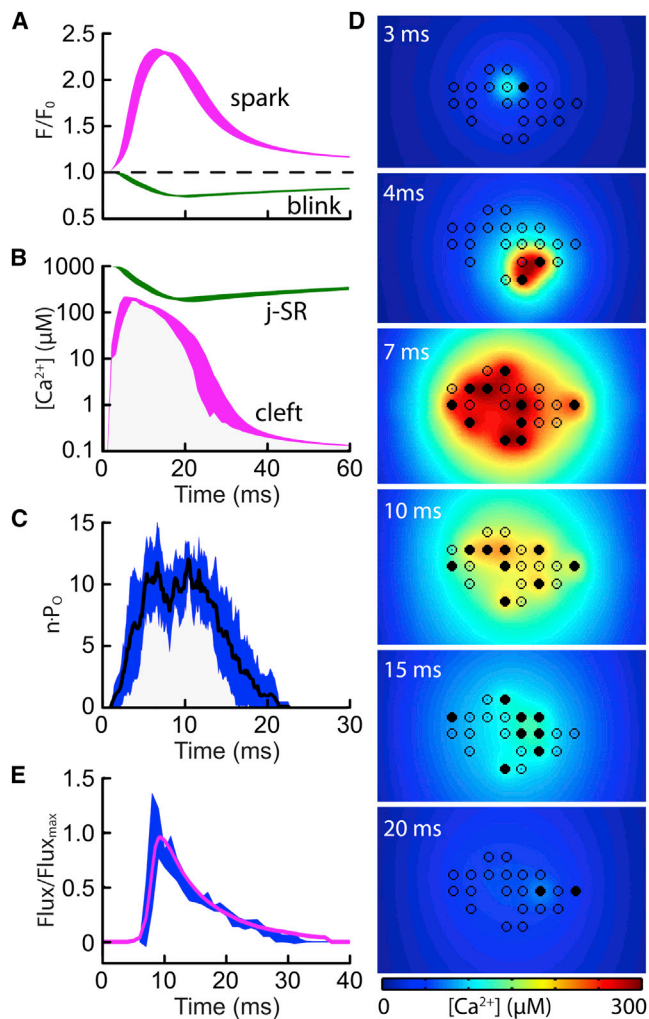


**FIGURE 4** RyR cluster behavior during  $\text{Ca}^{2+}$  sparks. (A)  $\text{Ca}^{2+}$  spark and  $\text{Ca}^{2+}$  blink time courses for a cluster of 21 RyRs with a distribution as shown in D. (B) Spatial mean of  $[\text{Ca}^{2+}]$  in the dyadic cleft and j-SR. (C) Numbers of open RyRs corresponding to the means in B. In A–C, line thickness shows the SD of 10 simulations. (D) Spatial distribution of  $[\text{Ca}^{2+}]$  in the dyad at several time points during a typical simulation. RyRs are located at the circles, with solid and open circles representing open and closed RyRs, respectively. (E) Simulated time course of j-SR  $\text{Ca}^{2+}$  flux (wide trace) compared to the  $\text{Ca}^{2+}$  flux calculated from experimental  $\text{Ca}^{2+}$  spark profiles (line) replotted from Soeller and Cannell (43).

phase of CICR that persisted for ~15 ms. By that time, j-SR  $[\text{Ca}^{2+}]$  had declined to ~10% of resting levels, which reduced the  $\text{Ca}^{2+}$  flux via open RyRs (Fig. 4 C) and consequently reduced local dyad  $[\text{Ca}^{2+}]$  to a point where regeneration decayed and the RyRs started to close. Once RyRs had closed,  $[\text{Ca}^{2+}]$  in the dyad cleft equilibrated with the bulk cytoplasm and  $\text{Ca}^{2+}$  in the j-SR was replenished by diffusion of  $\text{Ca}^{2+}$  from the n-SR. The decline in  $\text{Ca}^{2+}$  spark fluorescence was primarily due to  $\text{Ca}^{2+}$  diffusion in the cytoplasm and buffering, with SERCA reuptake playing a lesser role, as previously described (41,42). In this simulation, rat RyRs were distributed in a loose cluster, as depicted

in Fig. 4 D, which also shows the distribution of open RyRs and local dyad  $[\text{Ca}^{2+}]$  at several time points. The time course of  $\text{Ca}^{2+}$  flux from the dyad is shown in Fig. 4 E and is in good agreement with that calculated from  $\text{Ca}^{2+}$  spark flux reconstructions (43). Therefore the model reproduces all of the major features of  $\text{Ca}^{2+}$  sparks and blinks with reasonable accuracy.

### Termination of $\text{Ca}^{2+}$ sparks

Termination of RyR activity resulted principally from the steep  $\text{Ca}^{2+}$  dependence of RyR closed time (Fig. 2 C). If the opening rate of RyRs is sufficiently low, the open RyR(s) that is (are) supporting local dyad  $[\text{Ca}^{2+}]$  may close before the closed RyRs reopen to sustain CICR. We have termed this process induction decay (24), because it reflects the gradual loss of the activating  $\text{Ca}^{2+}$  induction process in CICR, which is responsible for the initial rapid rise in RyR  $P_o$ . Thus, the termination of RyR activity depends on RyR sensitivity to  $[\text{Ca}^{2+}]$  in the dyad cleft, as well as the time course of j-SR depletion. For rat RyRs, the minimum dyad  $[\text{Ca}^{2+}]$  that could sustain CICR was ~50  $\mu\text{M}$  (Fig. 4 B). RyRs from sheep exhibited  $P_o$  and opening rates that were ~40-fold higher than the corresponding values for rat RyRs at 10  $\mu\text{M}$   $\text{Ca}^{2+}$  (Fig. 2, B and C, respectively). Fig. 5 compares the mean response of models incorporating

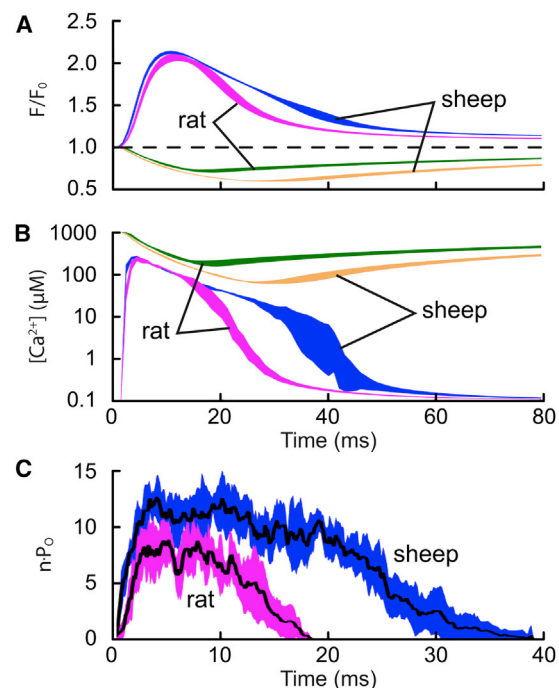


**FIGURE 5** Effect of RyR  $\text{Ca}^{2+}$  sensitivity on  $\text{Ca}^{2+}$  spark activation and termination. (A) Mean time courses of  $\text{Ca}^{2+}$  spark and blink signals generated using a square cluster of 16 RyRs with  $\text{Ca}^{2+}$ -activation kinetics derived from rat ( $n = 10$ ) and sheep data ( $n = 3$ ). (B) Corresponding spatial means of  $[\text{Ca}^{2+}]$  in the dyadic cleft and j-SR. (C) Number of open RyRs for rat and sheep  $\text{Ca}^{2+}$ -spark simulations, showing the mean (line)  $\pm$  SD, (wide trace).

RyRs (organized as a square cluster of 16 RyRs) from rat and sheep to a DHPR trigger. The computed time course of  $\text{Ca}^{2+}$  sparks (Fig. 5 A) show a similar rate of rise for rat (magenta) and sheep (blue) but a longer decay phase for sheep ( $\text{Ca}^{2+}$  spark parameters are given in Table 1.). The corresponding computed  $[\text{Ca}^{2+}]$  in the dyad cleft and j-SR and the RyR  $P_o$  are shown in Fig. 5, B and C, respectively. Both rat and sheep showed similar initiation of RyR activity and maximal  $P_o$ . However, sheep RyR activity was sustained for ~40 ms compared to ~18 ms for rat RyR activity. This is because with RyRs from sheep, the minimum dyad  $\text{Ca}^{2+}$  level that could sustain CICR was ~10  $\mu\text{M}$  (Fig. 5 B), which was fivefold lower than the corresponding value for rat RyRs, and it took approximately twice as long for the dyad  $[\text{Ca}^{2+}]$  to decline to this lower threshold. This different behavior may reflect physiological adaptation to the very different heart rates seen in these species (i.e., to have a shorter duration of SR release in rat RyRs). Even with more  $\text{Ca}^{2+}$  sensitive sheep RyRs, the combination of the limited j-SR volume and j-SR  $\text{Ca}^{2+}$  buffering capacity ensures that closure by induction decay occurs on the timescale of a  $\text{Ca}^{2+}$  spark.

The role of luminal regulation of RyR  $P_o$  was examined using gating data derived from Fig. 2. j-SR  $[\text{Ca}^{2+}]$  of 1 mM resulted in the RyR opening rate varying as cytoplasmic  $[\text{Ca}^{2+}]^{1.9}$  compared to  $[\text{Ca}^{2+}]^{2.8}$ . Opening rates at intermediate j-SR  $[\text{Ca}^{2+}]$  were given by linear interpolation. This RyR regulation by j-SR  $[\text{Ca}^{2+}]$  in our model produced almost no change in  $\text{Ca}^{2+}$  spark and blink morphology (Table 1, rows 2 and 3). From these measurements, we conclude that regulation of RyR gating by  $\text{Ca}^{2+}$  in the j-SR may not be a major factor in determining the spatiotemporal properties of  $\text{Ca}^{2+}$  sparks and blinks.

## Effects of RyR organization and dyad size

The role of local nanoscopic  $[\text{Ca}^{2+}]$  gradients in maintaining regeneration in CICR is illustrated in Fig. 6 A, which shows two arrangements of 18 RyRs as either two adjacent groups or one large group with every other RyR removed. Wherever there is a gap between adjacent RyRs, CICR terminated slightly earlier, but this had little effect on the amplitude of the  $\text{Ca}^{2+}$  spark (Fig. 6, A and B). This paradoxical result arises from the consequences of nanoscopic  $[\text{Ca}^{2+}]$  gradients within the dyad for determining both  $\text{Ca}^{2+}$  fluxes and CICR regeneration. As the RyRs become more separated, local CICR regeneration is weakened due to the spatial gradient of  $[\text{Ca}^{2+}]$  from each open RyR resulting in adjacent RyRs experiencing lower  $[\text{Ca}^{2+}]$  on average (leading to weakened regeneration and earlier termination). However, at the same time, the average flux associated with each RyR opening is increased due to a decreased local  $\text{Ca}^{2+}$  accumulation increasing the  $[\text{Ca}^{2+}]$  gradient that determines  $i_{\text{RyR}}$  (which offsets the former effect). Thus, nanoscopic gradients (illustrated in Figs. 4 D and 6 C) of  $[\text{Ca}^{2+}]$  within the RyR cluster play a key role in all phases of CICR regulation, from initiation to regeneration (which allows the j-SR to release a large fraction of its total  $\text{Ca}^{2+}$ ), as well as eventual termination. The dimensions of the dyad itself also have effects on CICR termination (as well as activation probability (44)). Fig. 6 D shows that a dyad with reduced area (but the same number of RyRs) results in a smaller  $\text{Ca}^{2+}$  spark that is abbreviated in time course.

Varying RyR cluster size between 2 and 36 RyRs revealed that  $\text{Ca}^{2+}$  spark properties were relatively insensitive to cluster size in clusters of more than nine RyRs (Table 1, rows 6–10). As noted previously, the shallow dependence

**TABLE 1** Morphological parameters of simulated sparks

| Condition               | $i_{\text{RyR}}$ (pA/mM) | $n_{\text{RyR}}$ | $F_{\text{max}}/F_o$ | $\Delta t(F_{\text{max}})$ (ms) | $\Delta F/\Delta t$ ( $\text{ms}^{-1}$ ) | $FWHM$ ( $\mu\text{m}$ ) | $FDHM$ (ms)    | $n$ |
|-------------------------|--------------------------|------------------|----------------------|---------------------------------|--|--------------------------|----------------|-----|
| Fig. 4                  | 0.6                      | 21               | $1.30 \pm 0.03$      | 14.3                            | $0.15 \pm 0.04$                          | $1.44 \pm 0.03$          | $19.6 \pm 1.6$ | 6   |
| Square RyR cluster      | 0.6                      | 16               | $1.04 \pm 0.06$      | 12.2                            | $0.144 \pm 0.017$                        | $1.40 \pm 0.03$          | $18.7 \pm 2.0$ | 17  |
| Luminal gating          | 0.6                      | 16               | $1.07 \pm 0.02$      | 12.9                            | $0.141 \pm 0.018$                        | $1.41 \pm 0.03$          | $19.0 \pm 1.4$ | 9   |
| Sheep RyRs              | 0.6                      | 16               | $1.07 \pm 0.01$      | 11.7                            | $0.161 \pm 0.007$                        | $1.42 \pm 0.02$          | $25.6 \pm 2.1$ | 3   |
| Narrower dyad           | 0.6                      | 16               | $0.86 \pm 0.02$      | 8                               | $0.184 \pm 0.022$                        | $1.07 \pm 0.02$          | $10.6 \pm 0.9$ | 4   |
| $n_{\text{RyR}}$ varied | 0.6                      | 36               | $1.21 \pm 0.01$      | 12                              | $0.175 \pm 0.003$                        | $1.39 \pm 0.02$          | $18.8 \pm 0.3$ | 3   |
|                         | 0.6                      | 16               | $1.04 \pm 0.06$      | 12.2                            | $0.144 \pm 0.017$                        | $1.40 \pm 0.03$          | $18.7 \pm 2.0$ | 17  |
|                         | 0.6                      | 9                | $0.95 \pm 0.02$      | 13.7                            | $0.113 \pm 0.003$                        | $1.42 \pm 0.03$          | $23.5 \pm 1.4$ | 3   |
|                         | 0.6                      | 4                | $0.68 \pm 0.06$      | 14.3                            | $0.071 \pm 0.003$                        | $1.38 \pm 0.04$          | $18.4 \pm 2.0$ | 6   |
|                         | 0.6                      | 2                | $0.47 \pm 0.05$      | 9.7                             | $0.069 \pm 0.003$                        | $1.32 \pm 0.03$          | $14.8 \pm 1.1$ | 9   |
| $i_{\text{RyR}}$ varied | 0.6                      | 16               | $1.04 \pm 0.06$      | 12.2                            | $0.144 \pm 0.017$                        | $1.40 \pm 0.03$          | $18.7 \pm 2.0$ | 17  |
|                         | 0.4                      | 16               | $0.89 \pm 0.07$      | 13.2                            | $0.108 \pm 0.035$                        | $1.37 \pm 0.05$          | $16.5 \pm 1.9$ | 6   |
|                         | 0.35                     | 16               | $0.87 \pm 0.07$      | 12.3                            | $0.107 \pm 0.025$                        | $1.35 \pm 0.03$          | $15.4 \pm 1.1$ | 7   |
|                         | 0.3                      | 16               | $0.83 \pm 0.07$      | 13.2                            | $0.098 \pm 0.018$                        | $1.36 \pm 0.02$          | $15.9 \pm 2.2$ | 10  |
|                         | 0.25                     | 16               | $0.74 \pm 0.16$      | 13.9                            | $0.079 \pm 0.023$                        | $1.37 \pm 0.05$          | $16.0 \pm 2.5$ | 10  |
|                         | 0.2                      | 16               | $0.52 \pm 0.27$      | 10.3                            | $0.067 \pm 0.022$                        | $1.31 \pm 0.07$          | $13.7 \pm 3.2$ | 9   |
|                         | 0.15                     | 16               | $0.38 \pm 0.14$      | 9.4                             | $0.057 \pm 0.007$                        | $1.30 \pm 0.07$          | $12.4 \pm 3.2$ | 12  |

First row is for the simulation depicted in Fig. 4. Subsequent rows show how spark properties change as various factors are altered, as indicated in the first column.  $i_{\text{RyR}}$  is the RyR single-channel  $\text{Ca}^{2+}$  current,  $n_{\text{RyR}}$  the number of RyRs in the simulated cluster,  $F_{\text{max}}/F_o$  the peak  $\text{Ca}^{2+}$  spark fluorescence change,  $\Delta t(F_{\text{max}})$  the time to peak of the  $\text{Ca}^{2+}$  spark,  $\Delta F/\Delta t$  the rate of rise of normalized fluorescence,  $FWHM$  the width of the spark at half-maximum amplitude, and  $FDHM$  the  $\text{Ca}^{2+}$  spark duration measured at half-maximum amplitude. Table gives mean  $\pm$  SD of  $n$  simulations.

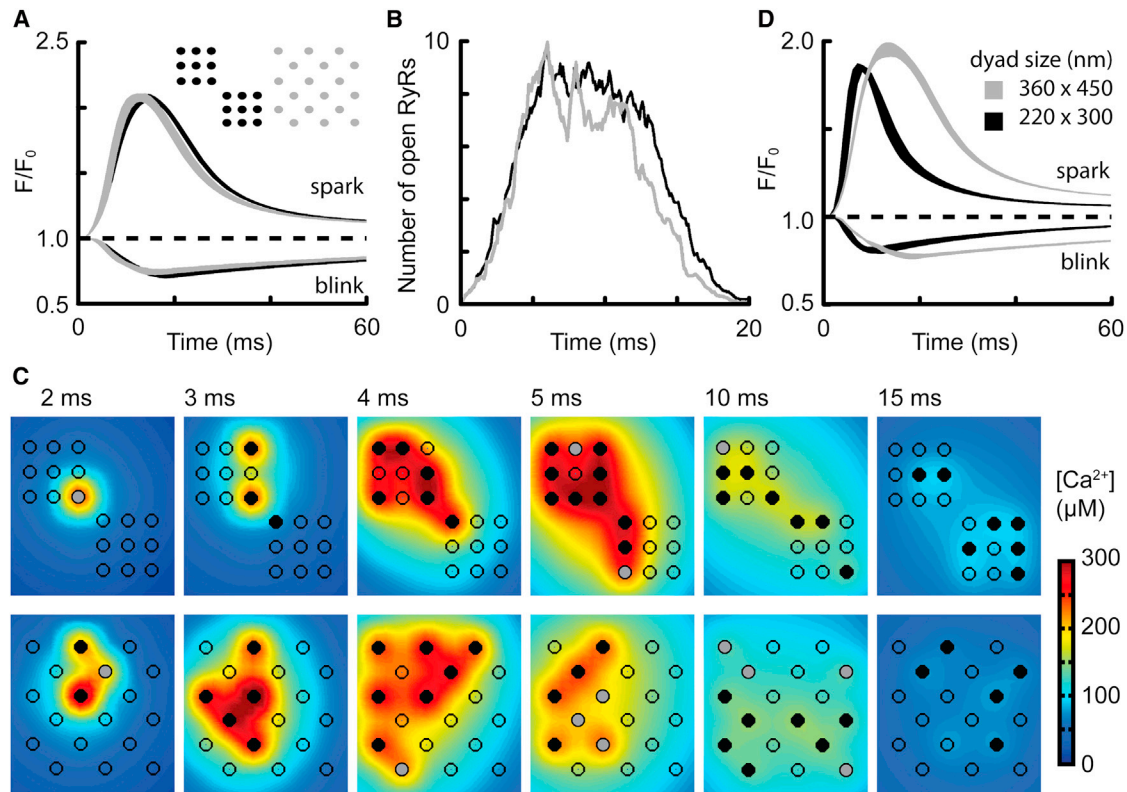


FIGURE 6 Intradyad geometric effects. (A)  $Ca^{2+}$  spark and blink time courses for two geometric arrangements of 18 RyRs. (Inset) Cluster organization with color key. (B) Evolution of mean  $P_o$  (shown as  $nP_o$ ) for the two clusters indicated in A. (C) Spatial distribution of  $[Ca^{2+}]$  in the dyad at several time points for the clusters shown in A. RyR states are depicted as described in Fig. 4 legend. (D) Effect of dyad dimensions. For a square cluster of 16 RyRs, the dyad space was set to the dimensions shown. Note that the smaller dyad results in faster  $Ca^{2+}$  spark termination but with a relatively small effect on amplitude.

of  $Ca^{2+}$  spark amplitude on the number of RyRs (24) arose from the effective diffusional resistance of the RyR open channels being less than the series diffusional resistances of the dyad cleft and SR.

### Restitution of $Ca^{2+}$ sparks after $Ca^{2+}$ release

The time course of  $Ca^{2+}$  spark recovery between spontaneous  $Ca^{2+}$  sparks (restitution) has been used to examine SR  $Ca^{2+}$  depletion, as well as possible RyR inactivation (20,25,45). Although our model contained no inactivated, adapted, or refractory states, the time course of recovery of  $Ca^{2+}$  spark amplitude (Fig. 7 A) and probability of evoking a second  $Ca^{2+}$  spark (Fig. 7 B) reproduced experimental observations (25). The explanation for the apparent refractory and restitution behavior lies in the extent to which the inductive regenerative phase of CICR can be supported by the partially depleted j-SR, and this is seen by comparing the time course of restitution of j-SR  $[Ca^{2+}]$ , peak  $F/F_0$ , and  $nP_o$  (Fig. 7 C).

The close agreement of our model with the reported restitution of  $Ca^{2+}$  spark amplitude (Fig. 7 A) was achieved without freely adjustable parameters.  $Ca^{2+}$  sparks had an apparent refractory period of  $\sim 70$  ms, and the second  $Ca^{2+}$

spark amplitude recovered to 80% of the initial  $Ca^{2+}$  spark amplitude in 130 ms. The restitution in the probability of triggering a second spark also depended on both the rate of occurrence of a triggering event (a spontaneous opening of either an RyR or a DHPR) and j-SR refilling, as shown by the dotted lines in Fig. 7 B. The  $Ca^{2+}$  spark restitution time course was determined by the rate of refilling of the j-SR, which in turn was constrained by the model fitting the rate of recovery of  $Ca^{2+}$  blinks (80% in 140 ms). j-SR refilling by diffusion from the n-SR and, to a lesser extent, local  $Ca^{2+}$  reuptake via SERCA was transduced via the local  $i_{RyR}$  to produce a more rapid recovery in  $nP_o$  than j-SR  $[Ca^{2+}]$  due to the power dependence of  $nP_o$  on dyad  $[Ca^{2+}]$  (Fig. 7 C).  $Ca^{2+}$  spark amplitude restitution also depended on the ability of the local  $Ca^{2+}$  flux ( $i_{RyR}$ ) to support the regenerative phase of CICR, with induction decay developing more rapidly at low j-SR  $[Ca^{2+}]$  (see below).

### Effect of RyR single-channel $Ca^{2+}$ flux

Recently, the effect of reducing RyR  $Ca^{2+}$  conductance and current ( $i_{RyR}$ ) with impermeant ions on  $Ca^{2+}$  spark amplitude and frequency has been reported (21). These data provide an important additional test of the model, and Fig. 7 D



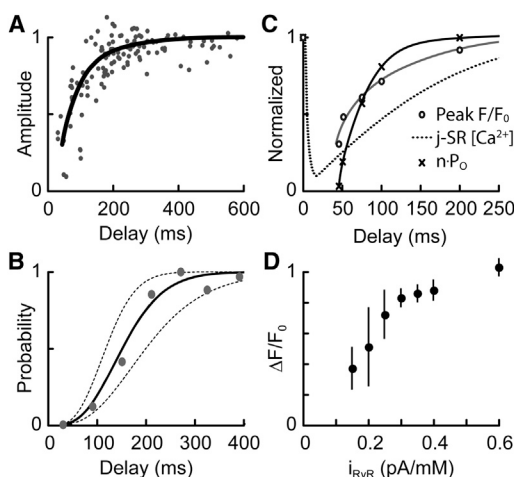


FIGURE 7  $\text{Ca}^{2+}$  spark restitution and  $i_{\text{RyR}}$  dependence. (A) Amplitude of the second  $\text{Ca}^{2+}$  spark (line) compared to experimental data (circles, replotted from Sobie et al. (25)). (B) Probability of triggering a second  $\text{Ca}^{2+}$  spark after various delays from the first. The trigger was assumed to be spontaneous RyR openings of 1 ms duration that occurred at intervals of 10 ms (left dashed line), 20 ms (solid line) and 40 ms (right dashed line). Data points (gray) are replotted from Sobie et al. (25). (C) Comparison of the time courses of j-SR  $[\text{Ca}^{2+}]$  (dashed line), peak fluorescence (open circles) and  $nP_o$  (crosses). (D) Effect of  $i_{\text{RyR}}$  on  $\text{Ca}^{2+}$  spark amplitude. Sparks were simulated in a dyad containing 16 RyRs in a  $4 \times 4$  array. The  $\text{Ca}^{2+}$  permeability of the RyR was varied and is expressed on the abscissa as  $\text{Ca}^{2+}$  current through the RyR in the presence of a 1 mM  $[\text{Ca}^{2+}]$  difference across the SR membrane. Data show the mean  $\pm$  SD for 6–17 simulations.

shows how  $\text{Ca}^{2+}$  spark amplitude varied as  $i_{\text{RyR}}$  was reduced to  $<0.6$  pA/mM. For  $i_{\text{RyR}}$  between 0.3 and 0.6 pA/mM,  $\text{Ca}^{2+}$  spark amplitude varied by 20%. However, when  $i_{\text{RyR}}$  was reduced to  $<0.3$  pA/mM the  $\text{Ca}^{2+}$  spark amplitude decreased more rapidly, reaching a  $\Delta F/F_o$  of 0.4 at 0.15 pA/mM, in reasonable agreement with the data of Guo et al. (21). Reducing  $i_{\text{RyR}}$  also hastened the onset of induction decay, resulting in a reduced time to peak for the resulting smaller-amplitude  $\text{Ca}^{2+}$  spark (Table 1, rows 15–17). In this regime,  $\text{Ca}^{2+}$  spark amplitude became more variable (as seen by the length of the error bars) as stochastic gating effects became relatively more important.

## DISCUSSION

The computer simulations presented here are based upon our best synthesis of available data on RyR gating, dyad geometry, and  $\text{Ca}^{2+}$  buffering. Although future work may lead to refinement of the geometry and parameters used, the model has given useful insight into the (likely) factors that determine the time course of SR  $\text{Ca}^{2+}$  release during  $\text{Ca}^{2+}$  sparks. Since the spatiotemporal evolution of  $\text{Ca}^{2+}$  sparks determines the rise of  $\text{Ca}^{2+}$  that activates contraction (35), this model can also give new insight into the factors that determine the cell-wide  $\text{Ca}^{2+}$  transient.

The simulations show that termination of RyR activity results from the spatiotemporal evolution of nanoscopic

$[\text{Ca}^{2+}]$  changes within the dyad, which are not properly captured by treating the junctional space of the dyad as a single compartment (46). As the  $\text{Ca}^{2+}$  flux via open RyRs starts to decrease, the decline in local dyad  $[\text{Ca}^{2+}]$  causes a decrease in the  $P_o$  of neighboring RyRs, which in turn reduces the total  $\text{Ca}^{2+}$  flux. This decrease in flux then further decreases cluster  $P_o$  (mainly via the RyR closed time), forming an inactivating process we called induction decay (24). Induction decay is essentially the reverse of the normal activating regenerative process of CICR and occurs due to the reduction in single-channel flux being unable to support regeneration of closed RyRs within the open time of adjacent RyRs. Our simulations show that the latency for induction decay to develop depends on the sensitivity of RyRs to dyad  $[\text{Ca}^{2+}]$ , as well as geometric factors such as the diameter of the dyad junction and number/organization of RyRs in the junction (Table 1 and Figs. 5 and 6).

A given dyad produces stereotyped  $\text{Ca}^{2+}$  sparks and blinks despite quite large stochastic variations in the number of open RyRs (compare the standard deviations in spark morphology in Fig. 4 A and Table 1 with the standard deviation in the number of open RyRs in Fig. 4 C). The reason for this behavior is that stochastic RyR gating is tempered by other, nonstochastic contributions to  $\text{Ca}^{2+}$  spark morphology, such as the series diffusion resistances of the dyad junction and the SR (when the RyRs have a  $\text{Ca}^{2+}$ -release flux ( $i_{\text{RyR}}$ )  $> \sim 0.3$  pA/mM). In addition, the  $\text{Ca}^{2+}$  spark fluorescence is smoothed by diffusion and buffering, which act as a low-pass filter for the stochastic RyR gating. The stereotypical nature of  $\text{Ca}^{2+}$  sparks in these simulations is less than the  $\text{Ca}^{2+}$  spark variation that occurs throughout the cell (36,47) but more than that observed at a single cytoplasmic release site (48). When  $i_{\text{RyR}}$  was  $<0.3$  pA/mM, the resulting  $\text{Ca}^{2+}$  sparks showed much greater variability due to increased stochastic noise. However, reports of highly variable or even quantized spark amplitudes (49,50) could be related to peripheral superclusters (51) or multiple dyadic junctions within the recording volume (12), which are uncertain factors not considered in this model. These possibilities could be tested with the 3D stochastic modeling approach presented here, but at this time, it is unknown how variable size groups of RyRs should be combined within a supercluster fed by a single piece of extended j-SR. Nevertheless, our simulations show that the actual organization of a fixed number of closely spaced RyRs sharing a single dyadic cleft (formed by a single SR junction) has quite small effects on  $\text{Ca}^{2+}$  release during a  $\text{Ca}^{2+}$  spark.

The limited effect on  $\text{Ca}^{2+}$  spark amplitude illustrates the remarkable resilience of dyad to moderate changes in geometry (although the geometry and RyR distribution have large effects on the ease with which CICR can be triggered (44)). The reduced diffusional resistance associated with reduced j-SR area accelerates CICR termination due to a more rapid collapse of nanoscopic CICR support, and at the same time, increases the rate at which  $\text{Ca}^{2+}$  leaves the dyad space (32).



Reduction in the j-SR area also reduced the width of the  $\text{Ca}^{2+}$  spark, as the indicator signal principally arises from  $\text{Ca}^{2+}$  that has left the dyad cleft edges. Varying the arrangement of RyRs from uniform squares of variable numbers of RyRs to looser arrangements (see Figs. 4 and 6) had relatively small effects on the amplitude of  $\text{Ca}^{2+}$  sparks and did not prevent termination of CICR by induction decay.

The robust nature of CICR activation and termination and the relative constancy of  $\text{Ca}^{2+}$  spark amplitude demonstrated here is underscored by the relative insensitivity of the release to the number of RyRs incorporated in the dyad at  $n > \sim 9$  RyRs (Table 1, rows 6–10, and (24)). Peripheral RyR clusters appear to contain  $\sim 14$  RyRs on average (51), and more central dyads should contain a somewhat larger number of RyRs (for review, see Cannell and Kong (12)). Although extensive electron microscopic tomography data are lacking, murine junctions appear to contain  $\sim 8$ –34 RyRs (52). This suggests that the dyad is not normally in a regime where  $\text{Ca}^{2+}$  spark amplitude is strongly influenced by the number of RyRs.

The rather limited effect of different RyR gating behavior associated with rat and sheep RyRs on  $\text{Ca}^{2+}$  spark amplitude might not be expected based on previous models. This result suggests that physiological modulation of RyR gating could have quite limited effects on  $\text{Ca}^{2+}$  spark amplitude, as the quantity released is mainly controlled by the ability of the local  $i_{\text{RyR}}$  to support regeneration. This hypothesis is compatible with the report by Guo et al. who found that RyR phosphorylation by protein kinase A had no effect on  $\text{Ca}^{2+}$  spark amplitude when SR load changes were controlled (53). Also, CaMKII RyR phosphorylation increases RyR  $\text{Ca}^{2+}$  sensitivity (54) and prolongs the release phase of  $\text{Ca}^{2+}$  sparks with little effect on  $\text{Ca}^{2+}$  spark amplitude (53). This is in general agreement with model behavior, as shown by the  $\text{Ca}^{2+}$  more  $\text{Ca}^{2+}$ -sensitive sheep RyR simulations (Fig. 5) where the onset of induction decay is delayed but  $\text{Ca}^{2+}$  sparks were only slightly increased in amplitude.

In connection with the above, it has been previously pointed out that a steady-state change in the amplitude of the  $\text{Ca}^{2+}$  transient would not be possible without a change in SR  $\text{Ca}^{2+}$  uptake (since time-averaged release must equal time-averaged uptake) (55). On the other hand, if pathological conditions lead to alterations in dyad geometry as a result of subcellular remodeling (such as the dyad morphing into multiple diffusionally connected subclusters of RyRs), our model shows that quite large effects on excitation-contraction coupling could result (from changes in triggering efficiency and altered  $\text{Ca}^{2+}$  spark termination). Such changes may help explain the paradoxical report of the development of a subpopulation of big resting  $\text{Ca}^{2+}$  sparks in a heart failure model without changes in SR  $\text{Ca}^{2+}$  content or expression levels of RyR, calsequestrin, SERCA2a, phospholamban, triadin, and junctin proteins (56). It should also be noted that there is evidence for the existence of superclu-

sters of RyRs on the cell surface (51), so the idea that RyRs may not always be packed into a single junctional cluster (as modeled here) is not without precedent. Thus, moderate pathological changes in dyad structure or distribution of RyR should not affect the average amplitude of  $\text{Ca}^{2+}$  sparks in the steady state, but by altering the ability of a trigger to start CICR, they could contribute to a change in  $\text{Ca}^{2+}$  transient time course and/or the development of spatial nonuniformities in  $\text{Ca}^{2+}$ , as seen in heart failure (see, e.g., Litwin et al. (57)).

Modulation of  $i_{\text{RyR}}$  has been used recently to probe the  $\text{Ca}^{2+}$  spark dependence on local  $\text{Ca}^{2+}$  flux and SR load (21). In those experiments, chemically skinned cells were exposed to 30 mM and 60 mM Tris, which produced a 20–40% reduction in  $i_{\text{RyR}}$  and  $\text{Ca}^{2+}$  spark amplitude and, importantly, also decreased  $\text{Ca}^{2+}$  spark time to peak (implying a more rapid onset of CICR termination). In our model, varying  $i_{\text{RyR}}$  over the range 0.15–0.35 pA caused similar variations in the amplitude as well as the time to peak of the computed  $\text{Ca}^{2+}$  sparks (Fig. 7 and Table 1, rows 11–17). This forms an additional independent test of our model (note that no other parameters were changed) and adds to our confidence that this stochastic 3D model captures the fundamental behavior of the dyad and shows that induction decay dominates CICR termination (24). From their experiments, Guo et al. (21) deduced that CICR termination during a  $\text{Ca}^{2+}$  spark was at least partly due to the loss of ability of  $i_{\text{RyR}}$  to support CICR, in accord with our demonstration of induction decay (24). A very recent review (58) describes induction decay as “pernicious attrition” but does not address the sufficiency and/or reliability of the falling RyR  $\text{Ca}^{2+}$  flux to limit CICR via the growth in RyR closed time that we show here. In any case, we view induction decay in CICR not as pernicious “pernicious,” but rather as a beneficial intrinsic component of CICR within dyads that necessarily limits SR  $\text{Ca}^{2+}$  release time course. We conclude that our stochastic 3D model captures the fundamental behavior of the dyad and that induction decay is sufficient to explain local termination of CICR without additional regulatory factors.

In summary, we show that a stochastic model that incorporates our current understanding of dyad structure and measurements of RyR gating in lipid bilayers reproduces the major features of  $\text{Ca}^{2+}$  sparks and blinks with reasonable accuracy and is able to reproduce additional properties such as the effect of changing  $i_{\text{RyR}}$  and the time course of restitution. The key to this behavior resides in the development of induction decay, as well as the time course of  $\text{Ca}^{2+}$  gradients between the dyadic space and j-SR. Changing RyR gating behavior to that of more  $\text{Ca}^{2+}$ -sensitive sheep RyRs had only small effects, suggesting that possible modulation of RyR gating by second messengers should be more effective in smaller couplons where regenerative support is weaker. Overall, the behavior of the model is reminiscent of the cluster-bomb model proposed by Stern, wherein local

depletion plus stochastic attrition in a small RyR cluster limits the amount of j-SR  $\text{Ca}^{2+}$  released (9). However, the problem inherent in stochastic attrition (i.e., a limit to the number of RyRs that can close by this mechanism within the timescale of a  $\text{Ca}^{2+}$  spark) is overcome by the automatic development of induction decay within the nanoscopic cellular architecture that forms the dyad.

## SUPPORTING MATERIAL

Three tables, one figure, methods, and references (58–72) are available at [http://www.biophysj.org/biophysj/supplemental/S0006-3495\(13\)00436-0](http://www.biophysj.org/biophysj/supplemental/S0006-3495(13)00436-0).

This work was supported by grants from the National Health and Medical Research Council and Hunter Medical Research Institute (D.L.) and the Royal Society (M.B.C.).

## REFERENCES

- Bers, D. M. 2002. Cardiac excitation-contraction coupling. *Nature*. 415:198–205.
- Meissner, G., E. Rousseau, ..., K. A. Anderson. 1988. Biochemical characterization of the  $\text{Ca}^{2+}$  release channel of skeletal and cardiac sarcoplasmic reticulum. *Mol. Cell. Biochem.* 82:59–65.
- Inui, M., and S. Fleischer. 1988. Purification of  $\text{Ca}^{2+}$  release channel (ryanodine receptor) from heart and skeletal muscle sarcoplasmic reticulum. *Methods Enzymol.* 157:490–505.
- Fabiato, A. 1983. Calcium-induced release of calcium from the cardiac sarcoplasmic reticulum. *Am. J. Physiol.* 245:C1–C14.
- Cannell, M. B., J. R. Berlin, and W. J. Lederer. 1987. Effect of membrane potential changes on the calcium transient in single rat cardiac muscle cells. *Science*. 238:1419–1423.
- Barcenas-Ruiz, L., and W. G. Wier. 1987. Voltage dependence of intracellular  $[\text{Ca}^{2+}]_i$  transients in guinea pig ventricular myocytes. *Circ. Res.* 61:148–154.
- Picht, E., A. V. Zima, ..., D. M. Bers. 2011. Dynamic calcium movement inside cardiac sarcoplasmic reticulum during release. *Circ. Res.* 108:847–856.
- Cheng, H., W. J. Lederer, and M. B. Cannell. 1993. Calcium sparks: elementary events underlying excitation-contraction coupling in heart muscle. *Science*. 262:740–744.
- Stern, M. D. 1992. Theory of excitation-contraction coupling in cardiac muscle. *Biophys. J.* 63:497–517.
- Cannell, M. B., H. Cheng, and W. J. Lederer. 1995. The control of calcium release in heart muscle. *Science*. 268:1045–1049.
- López-López, J. R., P. S. Shacklock, ..., W. G. Wier. 1995. Local calcium transients triggered by single L-type calcium channel currents in cardiac cells. *Science*. 268:1042–1045.
- Cannell, M. B., and C. H. T. Kong. 2012. Local control in cardiac E-C coupling. *J. Mol. Cell. Cardiol.* 52:298–303.
- Stern, M. D., and H. Cheng. 2004. Putting out the fire: what terminates calcium-induced calcium release in cardiac muscle? *Cell Calcium*. 35:591–601.
- Lukyanenko, V., T. F. Wiesner, and S. Györke. 1998. Termination of  $\text{Ca}^{2+}$  release during  $\text{Ca}^{2+}$  sparks in rat ventricular myocytes. *J. Physiol.* 507:667–677.
- Koh, X., B. Srinivasan, ..., A. Levchenko. 2006. A 3D Monte Carlo analysis of the role of dyadic space geometry in spark generation. *Biophys. J.* 90:1999–2014.
- Valdivia, H. H., J. H. Kaplan, ..., W. J. Lederer. 1995. Rapid adaptation of cardiac ryanodine receptors: modulation by  $\text{Mg}^{2+}$  and phosphorylation. *Science*. 267:1997–2000.
- Keizer, J., and L. Levine. 1996. Ryanodine receptor adaptation and  $\text{Ca}^{2+}$ -induced  $\text{Ca}^{2+}$  release-dependent  $\text{Ca}^{2+}$  oscillations. *Biophys. J.* 71:3477–3487.
- Sobie, E. A., K. W. Dilly, ..., M. S. Jafri. 2002. Termination of cardiac  $\text{Ca}^{2+}$  sparks: an investigative mathematical model of calcium-induced calcium release. *Biophys. J.* 83:59–78.
- Marx, S. O., J. Gaburjakova, ..., A. R. Marks. 2001. Coupled gating between cardiac calcium release channels (ryanodine receptors). *Circ. Res.* 88:1151–1158.
- Ramay, H. R., O. Z. Liu, and E. A. Sobie. 2011. Recovery of cardiac calcium release is controlled by sarcoplasmic reticulum refilling and ryanodine receptor sensitivity. *Cardiovasc. Res.* 91:598–605.
- Guo, T., D. Gillespie, and M. Fill. 2012. Ryanodine receptor current amplitude controls  $\text{Ca}^{2+}$  sparks in cardiac muscle. *Circ. Res.* 111:28–36.
- Zima, A. V., E. Picht, ..., L. A. Blatter. 2008. Termination of cardiac  $\text{Ca}^{2+}$  sparks: role of intra-SR  $[\text{Ca}^{2+}]$ , release flux, and intra-SR  $\text{Ca}^{2+}$  diffusion. *Circ. Res.* 103:e105–e115.
- Shannon, T. R., T. Guo, and D. M. Bers. 2003.  $\text{Ca}^{2+}$  scraps: local depletions of free  $[\text{Ca}^{2+}]$  in cardiac sarcoplasmic reticulum during contractions leave substantial  $\text{Ca}^{2+}$  reserve. *Circ. Res.* 93:40–45.
- Laver, D. R., C. H. T. Kong, ..., M. B. Cannell. 2013. Termination of calcium-induced calcium release by induction decay: an emergent property of stochastic channel gating and molecular scale architecture. *J. Mol. Cell. Cardiol.* 54:98–100.
- Sobie, E. A., L.-S. Song, and W. J. Lederer. 2005. Local recovery of  $\text{Ca}^{2+}$  release in rat ventricular myocytes. *J. Physiol.* 565:441–447.
- Franzini-Armstrong, C. 2009. Architecture and regulation of the  $\text{Ca}^{2+}$  delivery system in muscle cells. *Appl. Physiol. Nutr. Metab.* 34:323–327.
- Fawcett, D. W., and N. S. McNutt. 1969. The ultrastructure of the cat myocardium. I. Ventricular papillary muscle. *J. Cell Biol.* 42:1–45.
- Forbes, M. S., and E. E. van Neil. 1988. Membrane systems of guinea pig myocardium: ultrastructure and morphometric studies. *Anat. Rec.* 222:362–379.
- Forssmann, W. G., and L. Girardier. 1970. A study of the T system in rat heart. *J. Cell Biol.* 44:1–19.
- Mejía-Alvarez, R., C. Kettlun, ..., M. Fill. 1999. Unitary  $\text{Ca}^{2+}$  current through cardiac ryanodine receptor channels under quasi-physiological ionic conditions. *J. Gen. Physiol.* 113:177–186.
- Kettlun, C., A. González, ..., M. Fill. 2003. Unitary  $\text{Ca}^{2+}$  current through mammalian cardiac and amphibian skeletal muscle ryanodine receptor channels under near-physiological ionic conditions. *J. Gen. Physiol.* 122:407–417.
- Soeller, C., and M. B. Cannell. 1997. Numerical simulation of local calcium movements during L-type calcium channel gating in the cardiac dyad. *Biophys. J.* 73:97–111.
- Laver, D. R. 2007.  $\text{Ca}^{2+}$  stores regulate ryanodine receptor  $\text{Ca}^{2+}$  release channels via luminal and cytosolic  $\text{Ca}^{2+}$  sites. *Clin. Exp. Pharmacol. Physiol.* 34:889–896.
- Laver, D. R., and B. N. Honen. 2008. Luminal  $\text{Mg}^{2+}$ , a key factor controlling RYR2-mediated  $\text{Ca}^{2+}$  release: cytoplasmic and luminal regulation modeled in a tetrameric channel. *J. Gen. Physiol.* 132:429–446.
- Cannell, M. B., H. Cheng, and W. J. Lederer. 1994. Spatial non-uniformities in  $[\text{Ca}^{2+}]_i$  during excitation-contraction coupling in cardiac myocytes. *Biophys. J.* 67:1942–1956.
- Cheng, H., M. R. Lederer, ..., M. B. Cannell. 1996. Calcium sparks and  $[\text{Ca}^{2+}]_i$  waves in cardiac myocytes. *Am. J. Physiol.* 270:C148–C159.
- Wang, S. Q., L. S. Song, ..., H. Cheng. 2001.  $\text{Ca}^{2+}$  signalling between single L-type  $\text{Ca}^{2+}$  channels and ryanodine receptors in heart cells. *Nature*. 410:592–596.
- Zima, A. V., E. Picht, D. M. Bers, and L. A. Blatter. 2008. Termination of cardiac  $\text{Ca}^{2+}$  sparks: role of intra-SR  $[\text{Ca}^{2+}]$ , release flux, and intra-SR  $\text{Ca}^{2+}$  diffusion. *Circ. Res.* 103:e105–e115.

39. Brochet, D. X., D. Yang, ..., H. Cheng. 2005.  $\text{Ca}^{2+}$  blinks: rapid nanoscopic store calcium signaling. *Proc. Natl. Acad. Sci. USA*. 102:3099–3104.
40. Kong, C. H. T., D. R. Laver, and M. B. Cannell. 2013. Extraction of sub-microscopic Ca fluxes from blurred and noisy fluorescent indicator images with a detailed model fitting approach. *PLOS Comput. Biol.* 9:e1002931–e1002937.
41. Cheng, H., M. B. Cannell, and W. J. Lederer. 1995. Partial inhibition of  $\text{Ca}^{2+}$  current by methoxyverapamil (D600) reveals spatial nonuniformities in  $[\text{Ca}^{2+}]_i$  during excitation-contraction coupling in cardiac myocytes. *Circ. Res.* 76:236–241.
42. Santana, L. F., E. G. Kranias, and W. J. Lederer. 1997. Calcium sparks and excitation-contraction coupling in phospholamban-deficient mouse ventricular myocytes. *J. Physiol.* 503:21–29.
43. Soeller, C., and M. B. Cannell. 2002. Estimation of the sarcoplasmic reticulum  $\text{Ca}^{2+}$  release flux underlying  $\text{Ca}^{2+}$  sparks. *Biophys. J.* 82:2396–2414.
44. Cannell, M. B., and C. Soeller. 1997. Numerical analysis of ryanodine receptor activation by L-type channel activity in the cardiac muscle diad. *Biophys. J.* 73:112–122.
45. Sobie, E. A., and W. J. Lederer. 2012. Dynamic local changes in sarcoplasmic reticulum calcium: physiological and pathophysiological roles. *J. Mol. Cell. Cardiol.* 52:304–311.
46. Higgins, E. R., P. Goel, ..., J. Sneyd. 2007. Modelling calcium microdomains using homogenisation. *J. Theor. Biol.* 247:623–644.
47. Cheng, H., L. S. Song, ..., M. D. Stern. 1999. Amplitude distribution of calcium sparks in confocal images: theory and studies with an automatic detection method. *Biophys. J.* 76:606–617.
48. Bridge, J. H., P. R. Ershler, and M. B. Cannell. 1999. Properties of  $\text{Ca}^{2+}$  sparks evoked by action potentials in mouse ventricular myocytes. *J. Physiol.* 518:469–478.
49. Wang, S. Q., M. D. Stern, ..., H. Cheng. 2004. The quantal nature of  $\text{Ca}^{2+}$  sparks and in situ operation of the ryanodine receptor array in cardiac cells. *Proc. Natl. Acad. Sci. USA*. 101:3979–3984.
50. Shen, J.-X., S. Wang, ..., H. Cheng. 2004. Polymorphism of  $\text{Ca}^{2+}$  sparks evoked from in-focus  $\text{Ca}^{2+}$  release units in cardiac myocytes. *Biophys. J.* 86:182–190.
51. Baddeley, D., I. D. Jayasinghe, ..., C. Soeller. 2009. Optical single-channel resolution imaging of the ryanodine receptor distribution in rat cardiac myocytes. *Proc. Natl. Acad. Sci. USA*. 106:22275–22280.
52. Hayashi, T., M. E. Martone, ..., M. Hoshijima. 2009. Three-dimensional electron microscopy reveals new details of membrane systems for  $\text{Ca}^{2+}$  signaling in the heart. *J. Cell Sci.* 122:1005–1013.
53. Guo, T., T. Zhang, ..., D. M. Bers. 2006.  $\text{Ca}^{2+}$ /calmodulin-dependent protein kinase II phosphorylation of ryanodine receptor does affect calcium sparks in mouse ventricular myocytes. *Circ. Res.* 99:398–406.
54. Wehrens, X. H. T., S. E. Lehnart, ..., A. R. Marks. 2004.  $\text{Ca}^{2+}$ /calmodulin-dependent protein kinase II phosphorylation regulates the cardiac ryanodine receptor. *Circ. Res.* 94:e61–e70.
55. Dibb, K. M., H. K. Graham, ..., A. W. Trafford. 2007. Analysis of cellular calcium fluxes in cardiac muscle to understand calcium homeostasis in the heart. *Cell Calcium*. 42:503–512.
56. Shorofsky, S. R., R. Aggarwal, ..., C. W. Balke. 1999. Cellular mechanisms of altered contractility in the hypertrophied heart: big hearts, big sparks. *Circ. Res.* 84:424–434.
57. Litwin, S. E., D. Zhang, and J. H. Bridge. 2000. Dyssynchronous  $\text{Ca}^{2+}$  sparks in myocytes from infarcted hearts. *Circ. Res.* 87:1040–1047.
58. Gillespie, D., and M. Fill. 2013. Pernicious attrition and inter-RyR2 CICR current control in cardiac muscle. *J. Mol. Cell. Cardiol.* 58:53–58.
59. Laver, D. R., E. R. O'Neill, and G. D. Lamb. 2004. Luminal  $\text{Ca}^{2+}$ -regulated  $\text{Mg}^{2+}$  inhibition of skeletal RyRs reconstituted as isolated channels or coupled clusters. *J. Gen. Physiol.* 124:741–758.
60. Knollmann, B. C., N. Chopra, ..., K. Pfeifer. 2006. Casq2 deletion causes sarcoplasmic reticulum volume increase, premature  $\text{Ca}^{2+}$  release, and catecholaminergic polymorphic ventricular tachycardia. *J. Clin. Invest.* 116:2510–2520.
61. McLaughlin, S., N. Mulrine, ..., A. McLaughlin. 1981. Adsorption of divalent cations to bilayer membranes containing phosphatidylserine. *J. Gen. Physiol.* 77:445–473.
62. Protasi, F., C. Franzini-Armstrong, and B. E. Flucher. 1997. Coordinated incorporation of skeletal muscle dihydropyridine receptors and ryanodine receptors in peripheral couplings of BC3H1 cells. *J. Cell Biol.* 137:859–870.
63. Saito, A., M. Inui, ..., S. Fleischer. 1988. Ultrastructure of the calcium release channel of sarcoplasmic reticulum. *J. Cell Biol.* 107:211–219.
64. Soeller, C., and M. B. Cannell. 1999. Examination of the transverse tubular system in living cardiac rat myocytes by 2-photon microscopy and digital image-processing techniques. *Circ. Res.* 84:266–275.
65. Reference deleted in proof.
66. Rizzi, N., N. Liu, ..., S. G. Priori. 2008. Unexpected structural and functional consequences of the R33Q homozygous mutation in cardiac calsequestrin: a complex arrhythmogenic cascade in a knock in mouse model. *Circ. Res.* 103:298–306.
67. Franzini-Armstrong, C., F. Protasi, and V. Ramesh. 1999. Shape, size, and distribution of  $\text{Ca}^{2+}$  release units and couplons in skeletal and cardiac muscles. *Biophys. J.* 77:1528–1539.
68. Forbes, M. S., and N. Sperelakis. 1982. Bridging junctional processes in couplings of skeletal, cardiac, and smooth muscle. *Muscle Nerve*. 5:674–681.
69. Bers, D. M. 2001. Excitation-Contraction Coupling and Cardiac Contractile Force. Kluwer Academic, Dordrecht, The Netherlands.
70. Murphy, R. M., J. P. Mollica, ..., G. D. Lamb. 2011. Quantification of calsequestrin 2 (CSQ2) in sheep cardiac muscle and  $\text{Ca}^{2+}$ -binding protein changes in CSQ2 knockout mice. *Am. J. Physiol. Heart Circ. Physiol.* 300:H595–H604.
71. Ikemoto, N., B. Nagy, ..., J. Gergely. 1974. Studies on a metal-binding protein of the sarcoplasmic reticulum. *J. Biol. Chem.* 249:2357–2365.
72. Wu, X., and D. M. Bers. 2006. Sarcoplasmic reticulum and nuclear envelope are one highly interconnected  $\text{Ca}^{2+}$  store throughout cardiac myocyte. *Circ. Res.* 99:283–291.